ATLAS NOTE
ATLAS-CONF-2016-105
20th September 2016

Measurement of the azimuthal anisotropy of charged particles produced in 5.02 TeV Pb+Pb collisions with the ATLAS detector

The ATLAS Collaboration

Abstract

The data collected by the ATLAS experiment during the 2015 heavy ion LHC run offers new opportunities to probe properties of the Quark-Gluon Plasma at unprecedented high temperatures and densities. Study of the azimuthal anisotropy of produced particles not only constrains our understanding of initial conditions of nuclear collisions and soft particle collective dynamics, but also sheds light on jet-quenching phenomena via measurement of flow harmonics at high transverse momenta. A new ATLAS measurement of elliptic flow and higher-order Fourier harmonics of charged particles in Pb+Pb collisions at $\sqrt{s_{\mathrm{NN}}} = 5.02$ TeV in a wide range of transverse momenta, pseudorapidity ($|\eta| < 2.5$) and collision centrality is presented. These measurements are based on the Scalar Product and Two Particle Correlation methods. The measurements are compared with the results for Pb+Pb collisions at the lower energy.

ATLAS-CONF-2016-105
29 September 2016

1 Introduction

The properties of the QGP have been under thorough investigation since its discovery in Au+Au collisions at the Relativistic Heavy Ion Collider (RHIC) [1–4]. The existence of the Quark-Gluon Plasma (QGP) phase of nuclear matter, predicted by the Quantum Chromodynamics lattice calculations [5], has been confirmed by a wealth of experimental data. In particular, the properties related to the collective expansion of the QGP (e.g. the equation of state and shear viscosity) are inferred from measurements of azimuthal anisotropies of produced particles. It is expected that the azimuthal anisotropy results from large initial pressure gradients in the hot, dense matter created in the collisions. These pressure gradients transform the initial spatial anisotropies of nuclear collisions into momentum anisotropies of the final-state particle production, which are experimentally characterised by Fourier (flow) harmonics of the azimuthal angle distributions of produced particles [6, 7]. The discovery of large flow harmonics at RHIC, and more recently at much higher collision energy at the LHC [8–11], has significantly deepened our understanding of the QGP. In particular, the recent measurements of azimuthal anisotropy help to constrain the commonly used modelling of the dynamics of heavy-ion collisions based on relativistic viscous hydrodynamics. The hydrodynamic models assume that, shortly after the collision, the system is in a local equilibrium and forms a strongly interacting quark-gluon medium. Detailed investigations, based on hydrodynamics, have shown that the produced medium has properties similar to an almost ideal liquid characterised by a very low ratio of viscosity to entropy density, η/s. The goal of experimental heavy-ion physics is to improve our understanding of the strongly coupled QGP. Precise flow measurements are central to this because of their unique sensitivity to η/s.

The anisotropic distribution of azimuthal angles of produced particles is expanded as a Fourier series [12, 13]:

$$\frac{dN}{d\phi} = \frac{N_0}{2\pi}\left(1 + \sum_{n=1} 2v_n \cos\left[n\left(\phi - \Phi_n\right)\right]\right), \tag{1}$$

where ϕ is the azimuthal angle of the produced particles and the v_n and Φ_n are the magnitude and orientation of the n^{th} order azimuthal anisotropy. The coefficients, v_n, are commonly called "flow harmonics" due to their hydrodynamic origin. The v_n coefficients are functions of particle pseudorapidity (η), transverse momentum (p_{T}), and the degree of overlap between the colliding nuclei (centrality). Both the size of the collision overlap region and, for a given size, the number of interacting nucleons fluctuate from event to event. This generates so-called anisotropic flow fluctuations which arise from the initial fluctuations of the overlap region.

The first harmonic, v_1, is known as *directed flow* and refers to the sideward motion of fragments in ultra-relativistic nuclear collisions, and it carries information from the early stage of the collision. The most extensive studies are related to the second flow harmonic v_2, also known as *elliptic flow*. Elliptic flow is sensitive to the initial spatial asymmetry of the almond-shaped overlapping zone of colliding nuclei. The higher-order coefficients v_n, $n > 2$ are also important due to their sensitivity to the initial state geometry fluctuations and viscosity effects.

During the first operational period at the LHC (Run 1) Pb ions were collided at energy per nucleon $\sqrt{s_{\mathrm{NN}}}$ =2.76 TeV, which is about 13 times larger than the highest collision energy attained at RHIC in Au+Au collisions. ATLAS and other LHC experiments collected large samples of heavy-ion data allowing for extensive studies of the elliptic flow and higher-order Fourier coefficients. ATLAS measurements of flow harmonics were performed in broad regions of transverse momentum, pseudorapidity and event centrality, using the standard event-plane (EP) method [9], two-particle correlation function

(2PC) [10] and multi-particle cumulants [14]. Significant (non-zero) flow harmonics v_n up to n=6 were measured in Pb+Pb collisions at energy $\sqrt{s_{\rm NN}}$ =2.76 TeV, which indicate a very low shear viscosity of the QGP medium. Additionally, by comparing RHIC (STAR [15] and PHENIX [16]) and LHC (ATLAS [9], ALICE [17] CMS [18]) results it was found that for a given centrality class, v_n as function of $p_{\rm T}$ is essentially independent of collision energy. There is an initial rise of v_n with $p_{\rm T}$ up to about 3 GeVand then a drop off at higher values of $p_{\rm T}$, and only weak dependence for $p_{\rm T}$ > 8-9 GeV. As a function of centrality, there is similarly little variation with collision energy. The second harmonic, v_2, exhibits the most pronounced variation, rising to a maximum for mid-central, and then falling off for the most central collisions, where it has similar value to v_3. The higher ($n > 2$) harmonics show weaker dependence on centrality.

At the start of second operational period of the LHC (Run 2), in November and December of 2015, lead-lead collisions with higher collision energy per nucleon of $\sqrt{s_{\rm NN}}$ = 5.02 TeV were collected by the ATLAS experiment. The first results on v_n harmonics at this energy, obtained using the Scalar Product (SP) and two-particle correlations (2PC) methods, are presented in this note, using 5 μb^{-1} and 22 μb^{-1} of the integrated luminosity respectively. These results provide further opportunity to learn about the properties of the QGP, validate hydrodynamic models, study transport coefficients and the temperature dependence of physics observables including the ratio η/s.

The organisation of this note is as follows: Section 2 gives a brief overview of the ATLAS detector and its subsystems used in this analysis. Sections 3 and 4 describe the data sets, triggers and the offline selection criteria used to select events and reconstruct charged-particle tracks. Section 5 gives details of the scalar-product and two-particle correlation methods, which are used to measure the v_n. Section 6 describes the systematic uncertainties associated with the measured v_n. Section 7 presents the main results of the analysis, which are the $p_{\rm T}$, η and centrality dependence of the v_n. Section 8 gives a summary of the main results and observations.

2 Experimental Setup

The measurements were performed using the ATLAS [19] inner detector (ID), minimum-bias trigger scintillators (MBTS), calorimeter, zero-degree calorimeters (ZDC), and the trigger and data acquisition systems. The ID detects charged particles within the pseudorapidity range[1] $|\eta|$<2.5 using a combination of silicon pixel detectors, including the "insertable B-layer" (IBL) [20, 21] that was installed between Run 1 and Run 2, silicon microstrip detectors (SCT), and a straw-tube transition radiation tracker (TRT), all immersed in a 2 T axial magnetic field [22]. The MBTS system detects charged particles over $2.07 < |\eta| < 3.86$ using two scintillator-based hodoscopes on each side of the detector, positioned at $z = \pm 3.6$ m. These hodoscopes were rebuilt between Run 1 and Run 2. The ATLAS calorimeter system consists of a liquid argon (LAr) electromagnetic (EM) calorimeter covering $|\eta| < 3.2$, a steel–scintillator sampling hadronic calorimeter covering $|\eta| < 1.7$, a LAr hadronic calorimeter covering $1.5 < |\eta| < 3.2$, and two LAr electromagnetic and hadronic forward calorimeters (FCal) covering $3.2 < |\eta| < 4.9$. The ZDC's, situated at approximately ±140 m from the nominal IP, detect neutral particles, mostly neutrons and photons, with $|\eta|$>8.3. The ZDCs use tungsten plates as absorbers, and quartz rods sandwiched

[1] ATLAS uses a right-handed coordinate system with its origin at the nominal interaction point (IP) in the centre of the detector and the z-axis along the beam pipe. The x-axis points from the IP to the centre of the LHC ring, and the y-axis points upward. Cylindrical coordinates (r, ϕ) are used in the transverse plane, ϕ being the azimuthal angle around the z-axis. The pseudorapidity is defined in terms of the polar angle θ as $\eta = -\ln\tan(\theta/2)$.

between the tungsten plates as the active medium. The ATLAS trigger system [23] consists of a Level-1 (L1) trigger implemented using a combination of dedicated electronics and programmable logic, and a software-based high-level trigger (HLT).

3 Event Selection and Data Sets

The data used in this note were collected by a combination of two mutually exclusive triggers designed to deliver a minimum-bias sample. Events with relatively small impact parameter (central collisions) were recorded by requiring the total transverse energy deposited in the calorimeters at L1 to be above 50 GeV. On the other hand, for large impact parameters (peripheral events), the total transverse energy was limited to 50 GeV at L1 and additionally the presence of at least one neutron on either side in the ZDC and at least one track reconstructed in the ID were required. The total luminosity sampled by the minimum-bias triggers was 22 μb^{-1}. In the present note, the 2PC analysis utilizes the entire minimum-bias sample, while the SP analysis uses 5 μb^{-1}. In the offline analysis the z coordinate of the primary vertex is required to be within 10 cm of the nominal interaction point. The fraction of events containing more that one inelastic interaction (pile-up) is estimated to be at the level of 0.1%. Pile-up events were removed by exploiting the correlation between the transverse energy measured in the FCal and number of tracks associated with a primary vertex.

The minimum bias sample is divided into centrality classes. As the impact parameter is not measurable experimentally, the centrality selection is based on the strong monotonic correlation between the impact parameter and the transverse energy measured in the forward calorimeter, $\Sigma E_{\mathrm{T}}^{\mathrm{FCal}}$. The Glauber [24] model is used to obtain the mapping from the observed $\Sigma E_{\mathrm{T}}^{\mathrm{FCal}}$ to the elementary properties, such as the number of binary nucleon-nucleon interactions or the number of nucleons participating in the nuclear collision. The Glauber model provides also a correspondence between the $\Sigma E_{\mathrm{T}}^{\mathrm{FCal}}$ distribution and sampling fraction of the total inelastic Pb+Pb cross section, allowing the setting of the centrality percentiles. For this analysis a selection of the 80% most central collisions (i.e. centrality (0–80)%) is used to avoid any biases from diffraction or other processes that contribute significantly to very peripheral collisions (centrality (80–100)%). Figure 1 shows the distribution of $\Sigma E_{\mathrm{T}}^{\mathrm{FCal}}$ in data and thresholds for the selection of centrality intervals.

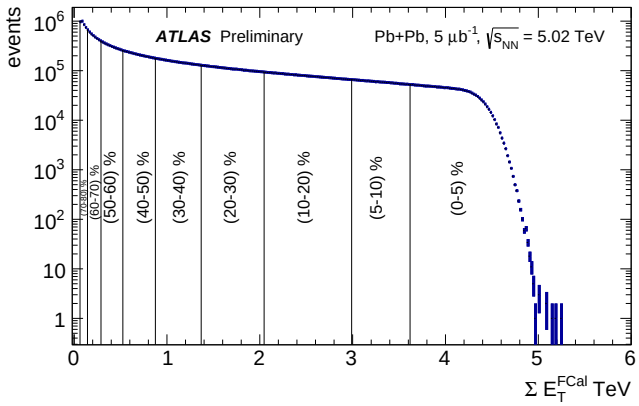

Figure 1: Distribution of the transverse energy in the FCal, $E_{\mathrm{T}}^{\mathrm{FCal}}$, for the min-bias event selection. The centrality bins are marked with vertical lines and labelled on the plot.

In order to study the performance of the ATLAS detector, a minimum-bias sample of $3 \cdot 10^5$ Pb-Pb MC events was generated using version 1.38b of HIJING [25]. The effect of flow is added after the generation using an "afterburner" [26] procedure in which the p_{T}, η and centrality dependence of the v_n as measured in the $\sqrt{s_{NN}}$ = 2.76 TeV Pb+Pb data is implemented. The generated sample is passed through a full simulation of the ATLAS detector using GEANT 4 [27], and the MC events are reconstructed by the same reconstruction algorithms as the data.

4 Track Selection

The charged-particle tracks are reconstructed from the signals in the ID. A special reconstruction procedure, optimized for tracking in dense environments, is used for this purpose [28]. In the analysis the set of reconstructed tracks is filtered using several selection criteria. The tracks are required to have $p_{\mathrm{T}} > 0.5$ GeV, $|\eta| < 2.5$, at least two pixel hits, with the additional requirement of a hit in the first pixel layer when one is expected [2], at least eight SCT hits, and at most one missing hit[3] in the SCT. In addition, the transverse (d_0) and longitudinal ($z_0 \sin(\theta)$) impact parameters of the track relative to the vertex are required to be less than 1 mm. The track-fit quality parameter χ^2/ndof is required to be less than 6. Finally, in order to remove tracks with mismeasured p_{T} due to interactions with the material or other effects, the track-fit χ^2 probability is required to be larger than 0.01 for tracks having $p_{\mathrm{T}} > 10$ GeV.

The MC sample is used to determine the track-reconstruction efficiency as a function of p_{T} and η , $\epsilon(p_{\mathrm{T}}, \eta)$. At mid-rapidity ($|\eta| < 1$) the reconstruction efficiency is ~70% at low p_{T} and increases to ~75% at higher p_{T}. For $|\eta| > 1$ the efficiency decreases to about (40–50)% depending on the p_{T}. The reconstruction efficiency depends weakly on the centrality for low p_{T} tracks, for which it is smaller in the most central events by about 4% as compared to mid-central and peripheral collisions. For tracks with $p_{\mathrm{T}} > 1$ GeV the dependence on centrality is less than 1%. The fraction of tracks that are not associated with stable generated MC particles, but are produced from random combinations of hits in the ID ("fake tracks"), is found to vary significantly depending on η. For $|\eta| < 1$, it is ~2% for low-p_{T} tracks in the most central (centrality (0–5)%) Pb+Pb events, and much below 1% for higher p_{T} in more peripheral collisions. In the forward part of the detector, especially for $1 < |\eta| < 2$ where detector services reside, the fake rate is up to 8% at low p_{T} and for the most central collisions. The fake rate drops rapidly for higher p_{T} and also decreases gradually towards more peripheral collisions so that it is almost negligible already in the (20–30)% centrality interval.

5 Analysis Procedure

Two analysis techniques are used to determine the flow harmonics: the 2PC method, which uses only the information from the tracking detectors, and the SP method, which uses in addition the FCal. In both approaches the differential flow harmonics are first obtained in narrow intervals of p_{T}, η and centrality. Integrated quantities are obtained by taking into account the track reconstruction efficiency, ϵ, and fake rate, f. A p_{T}-, η- and centrality-dependent weight factor $w = (1 - f)/\epsilon$ is applied to each track in the 2PC measurement and to scale each bin of the differential v_n distributions in the SP method.

[2] A hit is expected if the extrapolated track crosses an active region of a pixel module that has not been disabled.
[3] A hit is said to be missing when it is expected but not found.

5.1 Two particle correlation analysis

The 2PC method has been used extensively by ATLAS for correlation measurements [10, 29–33]. In the 2PC method, the distribution of particle pairs in relative azimuthal angle $\Delta\phi = \phi^a - \phi^b$ and pseudorapidity separation $\Delta\eta = \eta^a - \eta^b$ is measured. Here the labels a and b denote the two particles used to make the pair. They are conventionally called the "trigger" and "associated" particles, respectively. The two particles involved in the correlation measurement can be selected using various criteria, for example different p_{T} ranges (hard-soft correlations), different rapidity (forward-backward correlation), different charge combination (same-sign or opposite-sign correlation) or different particle species etc. In this analysis, the two particles are charged hadrons measured by the ATLAS tracking system, over the full azimuth and $|\eta| < 2.5$, resulting in a pair-acceptance coverage of ± 5.0 units in $\Delta\eta$.

In order to account for the detector acceptance effects, the correlation is constructed from the ratio of the distribution in which the trigger and associated particles are taken from the same event to the distribution in which the trigger and associated particles are taken from two different events. These two distributions are referred to as the "same-event" (S) or "foreground" distribution and the "mixed-event" or "background" (B) distribution, respectively, and the ratio is written as:

$$C(\Delta\eta, \Delta\phi) = \frac{S(\Delta\phi, \Delta\eta)}{B(\Delta\phi, \Delta\eta)}. \tag{2}$$

The same-event distribution includes both the physical correlations and correlations arising from detector acceptance effects. On the other hand, the mixed-event distribution reflects only the effects of detector inefficiencies and non-uniformity, but contains no physical correlations, To ensure that the acceptance effects in the B distribution match closely in the S distribution, the B distribution is constructed from particles from two different events that have similar multiplicity and z-vertex. Furthermore, in order to account for the effects of tracking efficiency $\epsilon(p_{\mathrm{T}}, \eta)$, each pair is weighted by $\frac{1}{\epsilon(p_{\mathrm{T}}^a, \eta^a)\epsilon(p_{\mathrm{T}}^b, \eta^b)}$ for S and B. In the ratio C, the acceptance effects largely cancel out and only the physical correlations remain [34]. Typically, the two-particle correlations are used only to study the shape of the correlations in $\Delta\phi$, and are conveniently normalised. In this note, the normalisation of $C(\Delta\eta, \Delta\phi)$ is chosen such that the $\Delta\phi$-averaged value of $C(\Delta\eta, \Delta\phi)$ is unity for $|\Delta\eta| > 2$.

Figure 2 shows $C(\Delta\eta, \Delta\phi)$ for several centrality intervals for $2 < p_{\mathrm{T}}^{a,b} < 3$ GeV, where p_{T}^a and p_{T}^b label the p_{T} of the trigger and associated particles used in the correlation. In all cases a peak is seen in the correlation at $(\Delta\eta, \Delta\phi) \sim (0, 0)$. This peak arises from short-range correlations such as decays, Hanbury Brown and Twiss (HBT) correlations [35], or jet-fragmentation. The long-range (large $\Delta\eta$) correlations are the result of the global anisotropy of the event and are the focus of the study in this note.

To investigate the $\Delta\phi$ dependence of the long-range ($|\Delta\eta| > 2$) correlation in more detail, the projection on to the $\Delta\phi$ axis is constructed as follows:

$$C(\Delta\phi) = \frac{\int_2^5 d|\Delta\eta|\, S(\Delta\phi, |\Delta\eta|)}{\int_2^5 d|\Delta\eta|\, B(\Delta\phi, |\Delta\eta|)} \equiv \frac{S(\Delta\phi)}{B(\Delta\phi)}. \tag{3}$$

The $|\Delta\eta| > 2$ requirement is imposed to reject the near-side jet peak and focus on the long-range features of the correlation functions.

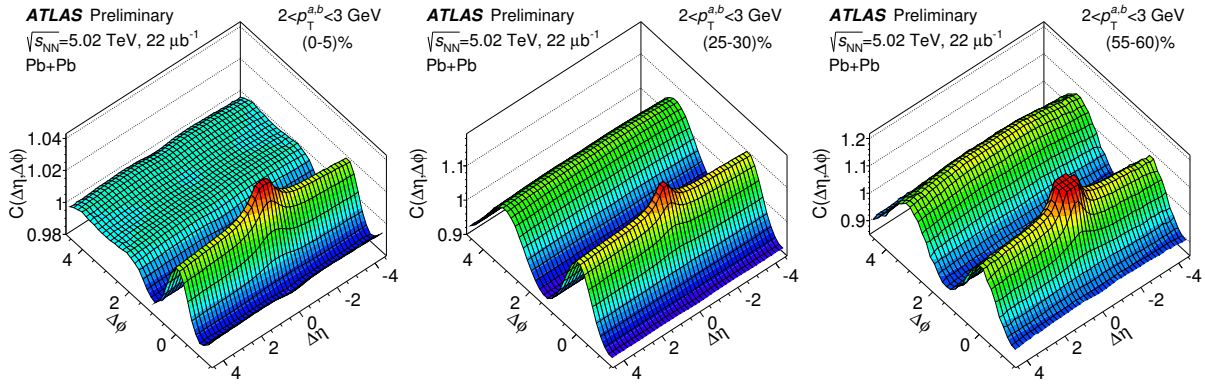

Figure 2: Two-particle correlation functions $C(\Delta\eta, \Delta\phi)$ in 5.02 TeV Pb+Pb collisions for $2<p_{\mathrm{T}}^{a,b}<3$ GeV. The left middle and right panels correspond to the (0–5)%, (25–30)% and (55–60)% centrality classes respectively.

In a similar fashion to the single-particle distribution Eq.(1), the 2PC can be expanded as a Fourier series:

$$C(\Delta\phi) = C_0\left(1 + \Sigma_{n=1}^{\infty} v_{n,n}(p_{\mathrm{T}}^a, p_{\mathrm{T}}^b)\cos(n\Delta\phi)\right). \tag{4}$$

If the two-particle distribution is simply the product of two single-particle distributions, then it can be shown that the Fourier coefficients of the 2PC factorize as:

$$v_{n,n}(p_{\mathrm{T}}^a, p_{\mathrm{T}}^b) = v_n(p_{\mathrm{T}}^a)v_n(p_{\mathrm{T}}^b) \tag{5}$$

The factorization of $v_{n,n}$ given by Eq. (5) is expected to break at high p_{T} where the anisotropy does not arise from flow. The factorization is also expected to break when the η separation between the particles is small, and short-range correlations dominate. However, the $|\Delta\eta|>2$ requirement removes most of such short-range correlations. In the phase-space region where Eq. (5) holds, the v_n (p_{T}^b) can be evaluated from the measured $v_{n,n}$ as:

$$v_n(p_{\mathrm{T}}^b) = \frac{v_{n,n}(p_{\mathrm{T}}^a, p_{\mathrm{T}}^b)}{v_n(p_{\mathrm{T}}^a)} = \frac{v_{n,n}(p_{\mathrm{T}}^a, p_{\mathrm{T}}^b)}{\sqrt{v_{n,n}(p_{\mathrm{T}}^a, p_{\mathrm{T}}^a)}}, \tag{6}$$

where in the denominator, the condition $v_{n,n}(p_{\mathrm{T}}^a, p_{\mathrm{T}}^a) = v_n^2(p_{\mathrm{T}}^a)$ is used. In this analysis, for most of the 2PC results the v_n (p_{T}^b) will be evaluated using Eq (6) with $0.5<p_{\mathrm{T}}^a<5.0$ GeV. The lower cutoff of 0.5 GeV on p_{T}^a comes from the range over which the measurements are done in this note (0.5–25 GeV). The upper cutoff on p_{T}^a is chosen to exclude high-p_{T} particles which predominantly come from jets and are not expected to obey Eq. (6).

Figure 3 shows one-dimensional 2PCs as a function of $\Delta\phi$ for $2<p_{\mathrm{T}}^{a,b}<3$ GeV and for several different centrality intervals. The correlations have been normalized to have a mean value (C_0 in Eq. (4)) of 1.0. The continuous line is a Fourier fit to the correlation (Eq. (4)) that includes harmonics up to n=6. The contribution of the individual $v_{n,n}$ are also shown. The modulation in the correlation about its mean value is the smallest in the most central events (top left panel) and increases towards mid-central events reaching a maximum in the (45–50)% centrality interval and then decreases. In central collisions, the $v_{2,2}$-$v_{4,4}$ are of comparable magnitude. But for other centralities, where the average collision geometry is elongated, the $v_{2,2}$ is significantly larger than the other $v_{n,n}$ for $n \geq 3$. In the central events the away-side peak is also much broader because all the significant harmonics are of similar magnitude, while in mid-central events the near and away-side peaks are quite symmetric as the $v_{2,2}$ dominates. In central and mid-central events, the near-side peak is larger than the away-side peak. However, for centralities

(60-80)% the away-side peak becomes larger due to the presence of a large negative $v_{1,1}$ component. This negative $v_{1,1}$ component in the peripheral 2PCs arises largely from dijets: while the near-side jet peak is rejected by the $|\Delta\eta|$>2 cut, the away-side jet position varies in $|\Delta\eta|$ from event to event, and cannot be rejected entirely. In the peripheral multiplicity intervals, the away-side jet significantly affects the 2PC. It produces a large negative $v_{1,1}$ and also affects the other harmonics by adding alternatingly positive and negative contributions to them: i.e. positive contribution to $v_{2,2}$, negative contribution to $v_{3,3}$, positive contribution to $v_{4,4}$ and so on. In peripheral events the $v_{n,n}$ are strongly biased by dijets especially at higher p_{T}. The presence of the jets also results in the breakdown of the factorization relation (Eq. (6)).

5.2 Scalar Product and Event Plane analysis

The SP method has been introduced by the STAR collaboration [36] and is further discussed in Ref. [13]. The SP method is very similar to the Event Plane method (EP) widely used in earlier analyses [9, 10]. It is superior to the EP as v_n {SP} is an estimator of $\sqrt{\langle v_n^2\rangle}$, independent of the detector resolution and acceptance, whereas $v_n\{EP\}$ produces a detector-dependent estimate of v_n that lies between $\langle v_n\rangle$ and $\sqrt{\langle v_n^2\rangle}$ [5, 37].

The SP method uses flow vectors defined as

$$Q_n = |Q_n|e^{in\Psi_n} = \frac{1}{S}\sum_{j=1,S} q_{n,j} = \frac{1}{S}\sum_{j=1,S} w_j e^{in\phi_j}, \tag{7}$$

where the sum runs over S particles in a single event, restricted to a selected region of phase space of (η, p_{T}). The ϕ_j is the particle azimuthal angle and n is the harmonic order. In this analysis the flow vectors are established separately for the two sides of the FCal and are denoted $Q_n^{N|P}$, where the N and P correspond to the two sides of the detector (N for $\eta < 0$ and P for $\eta > 0$). The sum in Eq. (7) in this case runs over the calorimeter towers of approximate granularity $\eta \times \phi = 0.1 \times 0.1$ and the weights w_i are linear functions of the E_{T} of the towers. The tower E_{T} is scaled so that the response, averaged over all events in the data-taking run, is identical for each tower in the η slice. A similar "flattening" procedure is applied when Q_n is calculated using charged-particle tracks. In this case the weight w_j is the inverse of the relative track-reconstruction efficiency, which is obtained from the data as the inverse of the track multiplicity in the narrow $\eta \times \phi = 0.1 \times 0.1$ interval, normalised such that the average efficiency in one η slice of 0.1 width is unity.

The values of v_n in this analysis are obtained as

$$v_{n,j}\{\mathrm{SP}\} = Re\frac{\langle q_{n,j}Q_n^{N|P*}\rangle}{\sqrt{\langle Q_n^N Q_n^{P*}\rangle}} = \frac{\langle |q_{n,j}||Q_n^{N|P}|cos[n(\phi_j - \Psi_n^{N|P})]\rangle}{\sqrt{\langle |Q_n^N||Q_n^P|cos[n(\Psi_n^N - \Psi_n^P)]\rangle}}, \tag{8}$$

where $q_{n,j}$ is the flow vector obtained for a small (η, p_{T}) interval (typically 0.1 in η and in p_{T} 0.1 GeV at low p_{T} and 1 GeV at higher p_{T}) using tracks, $Q_n^{N|P}$ is the flow vector obtained using either the N or P side of the FCal, chosen so that the η gap between the η of the $q_{n,j}$ interval and Q_n is maximised, the * denotes complex conjugation, the Ψ_n are estimates of the n-th order reacion-plane angles (Eq. (7)) and the angular brackets indicate an average over all events. In the rightmost expression in Eq.(8) it is assumed that the sine terms disappear. The inverse of the correction factor, $\sqrt{\langle Q_n^N Q_n^{P*}\rangle}$, (denominator in Eq. (8)) depends on the harmonic order and $\Sigma E_{\mathrm{T}}^{\mathrm{FCal}}$ as shown in Fig. 4.

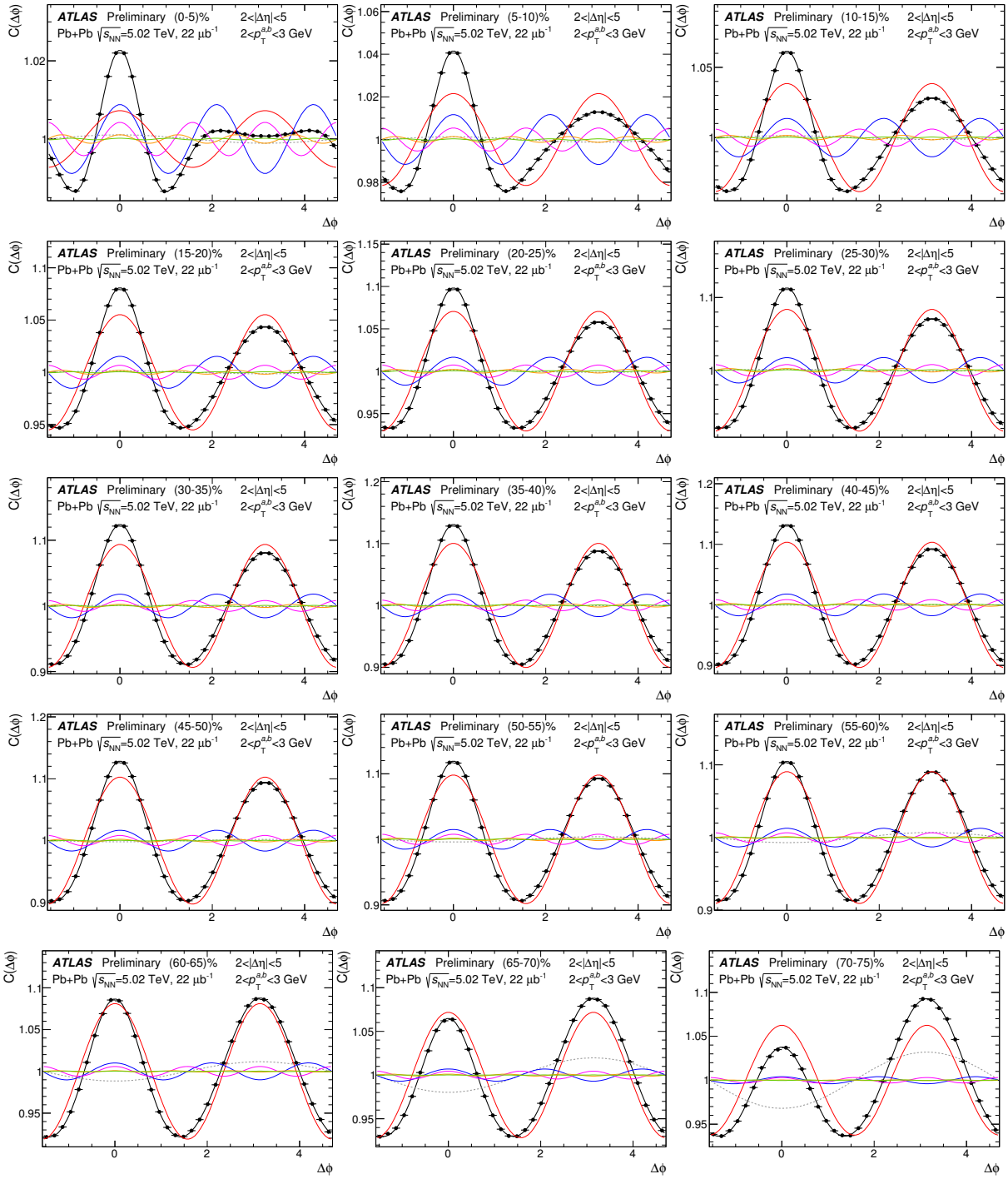

Figure 3: One dimensional two-particle correlation functions $C(\Delta\phi)$ in 5.02 TeV Pb+Pb collisions for $2<p_{\mathrm{T}}^{a,b}<3$ GeV(points). The solid-black line indicates a fit to Eq. (4) containing harmonics $v_{n,n}$ up to n=6. The dashed grey line shows the contribution of the $v_{1,1}$. The contributions of the $v_{2,2}$–$v_{6,6}$ are indicated by the coloured lines ($v_{2,2}$- red, $v_{3,3}$- blue, $v_{4,4}$- magenta, $v_{5,5}$-orange, $v_{6,6}$- green). Each panel corresponds to a different centrality class. The y-axis range for the different panels is different.

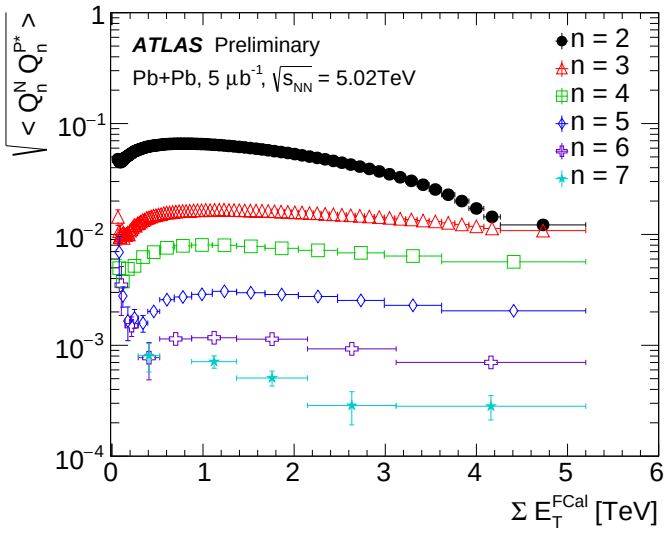

Figure 4: The dependence of the correction factor in the SP method, $\sqrt{\langle Q_n^N Q_n^{P*}\rangle}$, for all measured harmonics as a function of $\Sigma E_{\mathrm{T}}^{\mathrm{FCal}}$ binned according to the centrality bins definition.

In the Event Plane analysis the reference Q vectors are normalised to unity, $Q_n^{N|P} \to Q_n^{N|P}/|Q_n^{N|P}|$, before using them in Eq. (8). So the v_n estimate is obtained as

$$v_n\{\mathrm{EP}\} = Re\frac{\left\langle q_{n,j}\frac{Q_n^{N|P*}}{|Q_n^{N|P}|}\right\rangle}{\sqrt{\left\langle \frac{Q_n^N}{|Q_n^N|}\frac{Q_n^{P*}}{|Q_n^P|}\right\rangle}} = \frac{\langle cos[n(\phi_j - \Psi_n^{N|P})]\rangle}{\sqrt{\langle cos[n(\Psi_n^N - \Psi_n^P)]\rangle}}. \tag{9}$$

In this analysis the EP method is used only for the purpose of a direct comparison with the results obtained in Run 1, in which the EP method was used.

The analysis is performed in intervals of centrality. The v_n values are obtained in narrow bins of p_{T} and η, which are summed, taking into account tracking efficiency and fake rate, to obtain the integrated results.

6 Systematic Uncertainties

The systematic uncertainties of the measured v_n are evaluated by varying several aspects of the analysis. The uncertainties of the EP results are very similar to those for the SP results, and are not discussed separately. Similarly, some of the uncertainties are common in their origin between the EP/SP and the 2PC methods and are discussed together. The uncertainties are summarised in the Table 1 and 2 for the 2PC and SP/EP methods respectively. The following sources of uncertainties are considered:

- **Track selection:** The tracking selection cuts control the relative contribution of genuine charged particles and fake tracks entering the analysis. The stability of the results to the track selection is evaluated by varying the requirements imposed on the reconstructed tracks. For each variation, the entire analysis is repeated including the evaluation of the corresponding efficiencies and fake

rates. At the low p_{T} the variation in the v_n obtained from this procedure is most significant in the most central events, as the fake rate is largest in this region of phase space, and typically of the order of 5%. For higher p_{T}, changing the set of tracks used in the analysis has less influence on the measurement.

- **Tracking efficiency:** As mentioned above, the tracks are weighted by $1/\epsilon(p_{\mathrm{T}}, \eta)$ when calculating the v_n to account for the effects of the tracking efficiency. Uncertainties in the efficiency, resulting e.g. from an uncertainty of the detector material budget, need to be propagated into the measured v_n. This uncertainty is evaluated by varying the efficiency up and down within its uncertainties in a p_{T} dependent manner and re-evaluating the v_n. This contribution to the overall uncertainty is very small and amounts to less than 1% on average. This is because the change of efficiency cancels out in the differential $v_n(p_{\mathrm{T}})$ measurement, and for v_n integrated over p_{T}, the low-p_{T} particles dominate the measurement. It does not change significantly with centrality nor with the order of harmonics.

- **Uncertainty in the centrality determination:** A scale uncertainty on the flow harmonics comes from the uncertainty in the fraction of the total inelastic cross-section accepted by the trigger and the event selection criteria. It is evaluated by varying the centrality bin definitions, using the modified selections, which account for the 1% uncertainty in the sampled fraction of the cross-section. The changes in the v_n are largest in the peripheral-centrality intervals, for which the bin definitions are significantly changed when remapping the centralities. For v_2, a change of ∼0.8% (2PC) and ∼1.5% (SP) is also observed in the most central events. This is because the v_2 changes rapidly with centrality in central events, so slight variations in the centrality definition result in significant change in v_2. For v_3 this uncertainty varies from less than 0.5% over the (0–50)% centrality range to ∼5% in the (70–80)% centrality. For the higher-order harmonics $n > 3$ the uncertainty is less than 0.5% over the (0–50)% centrality range and increases to about 2% for more peripheral bins. The variation in the v_n when using these alternative centrality definitions is taken as a systematic uncertainty. Significant changes in the sample of events in the peripheral bins affect the v_7 at high p_{T}, indicating statistical instability of this measurement.

- **MC Closure:** The MC closure test consists of comparing the v_n^{true} obtained directly from the MC generated particles, and the v_n^{reco} obtained by applying the same procedures to the MC sample as are applied to the data. The analysis of MC events is done to evaluate the contributions of effects not corrected for in the data analysis. The two-particle correlation analysis is validated by measuring the $v_{n,n}$ of reconstructed particles in fully simulated HIJING events and comparing them to those obtained using the generated particles. For the SP method the $Q_n^{N|P}$ vectors are obtained with generated particles falling into the acceptance of the FCal ($3.2 < \eta < 4.8$). Due to the limited size of the MC sample, this contribution cannot be established for small v_n signals of high-order harmonics: v_6 and v_7, and v_4 and v_5 in more peripheral collisions. This uncertainty is at the level of a few percent, where the statistics permits a sensible estimate.

- **η asymmetry:** Due to the symmetry of the Pb+Pb collision system the event-averaged $\langle v_n(\eta)\rangle$ and $\langle v_n(-\eta)\rangle$ are expected to be equal. Any difference between the event-averaged v_n at $\pm\eta$ arises from residual detector non-uniformity. The difference between the v_n values measured in opposite hemispheres is treated as the systematic uncertainty quantifying a non-perfect detector performance. This uncertainty is in general very low (at the level of 1%) except for high-order harmonics v_5 and v_6 at high p_{T} and v_7 at all p_{T}. This uncertainty only contributes to the v_n values measured by the EP and SP methods. For the 2PC method, the residual non-uniformity is estimated by variation in the event-mixing procedure.

- **Residual sine term:** The ability of the detector to measure small v_n signals can be quantified by comparing the value of the v_n calculated as the real part of the flow vector product (SP) in Eq (8) to its imaginary part. The ratio $Im(SP)/v_n$ is taken as a contribution to the systematic uncertainty. As the values of $Im(SP)$ as well as the v_n are small, the limited numerical precision causes the ratio to vary significantly in bins of lower statistics. Therefore a common uncertainty for all tracks of $p_{\mathrm{T}} > 1.5$GeV is obtained and propagated to p_{T} bins above 1.5 GeV. The contribution from this source is ∼1% in most of the phase space, while for the higher harmonics (n=5, 6) and for the low p_{T} (0.5 − 0.6 GeV) it can reach 45% in the most central collisions. This uncertainty is only relevant for the v_n values measured by the EP and SP methods.
- **Variation of FCal acceptance in $Q_n^{N|P}$ estimation:** In order to quantify an uncertainty arising from FCal acceptance in $Q_n^{N|P}$ estimation, v_n harmonics are compared for two distinct FCal regions $3.2 < |\eta| < 4$ and $4 < |\eta| < 4.8$ used for the determination of the reference flow vector, Q_n. The differences in the v_n's are treated as the systematic uncertainty, which, similarly to the η symmetry, quantifies the ability of the detector to measure small signals. Accordingly, this contribution is small (of the order of about 1%) for v_2 and v_3 and starts growing for higher order harmonics up to about 80% for v_7. This uncertainty is only relevant to the v_n values measured by the EP and SP methods.
- **Event-mixing** As explained in Section 5.1, the 2PC analysis uses the event-mixing technique to estimate and correct for the detector acceptance effects. Potential systematic uncertainties in the v_n due to the residual pair-acceptance effects, which were not corrected by the mixed events, are evaluated following Ref. [10]. The resulting uncertainty on the v_2–v_5 is between 1–3%, and for v_6 is between 4–8% for most of the centrality and p_{T} ranges measured in this note. However, the uncertainties for v_4–v_6 are significantly larger for $p_{\mathrm{T}} < 0.7$ GeV where the v_n signals are quite small and very susceptible to acceptance effects. The uncertainties are also significantly larger for $p_{\mathrm{T}} > 10$ GeV where they are correlated with statistical uncertainties.

systematic sources	n harmonic	5 - 10 %		50 - 60 %	
		0.5–0.6 GeV	6–8 GeV	0.5–0.6 GeV	6–8 GeV
tracking cuts	v_2	8	3	1	1
	v_3	8	3	1	2
	v_4	11	4	3	4
	v_5	16	5	4	5
	v_6	16	8	4	8
efficiency variation	v_2	0.2	<0.1	0.2	<0.1
	v_3	0.2	0.2	0.3	0.7
	v_4	0.3	0.2	0.3	0.7
	v_5	0.2	<0.1	0.2	1.0
	v_6	4.8	11	4.2	0.9
centrality	v_2	1	1	1.5	<0.5
	v_3	0.5	0.5	3	10
	v_4	0.5	0.5	3	10
	v_5	0.5	0.5	3	10
	v_6	0.5	0.5	3	10
MC closure	v_2	6	3	3	1
	v_3	6	3	3	1
	v_4	5	5	5	5
	v_5	6	6	6	6
	v_6	10	10	10	10
event-mixing	v_2	1	1	1	1
	v_3	1	2	1	4
	v_4	5	6	3	6
	v_5	5	10	5	10
	v_6	50	15	50	15

Table 1: The systematic uncertainties associated with the 2PC v_n measurements for selected intervals of p_{T} and centrality. The contributions are experessed in %.

systematic sources	n harmonic	5 - 10 %		50 - 60 %	
		0.5 - 0.6 GeV	9 - 10 GeV	0.5 - 0.6 GeV	9 - 10 GeV
tracking cuts	v_2	5 (5)	0.2 (0.3)	0.1 (0.1)	0.3 (0.3)
	v_3	6 (6)	0.2 (0.2)	0.2 (0.1)	3 (2)
	v_4	6 (6)	0.4 (0.2)	3 (3)	1 (3)
	v_5	7 (9)	0.2 (1)	2 (2)	3 (2)
	v_6	14 (17)	1 (3)	3 (6)	3 (6)
	v_7	2 (12)	9 (3)	6 (26)	6 (26)
efficiency variation	v_2	0.2 (0.2)	<0.1 (<0.1)	0.2 (0.2)	<0.1 (<0.1)
	v_3	0.2 (0.2)	0.2 (<0.1)	0.3 (0.3)	0.7 (0.5)
	v_4	0.3 (0.3)	0.2 (0.3)	0.3 (0.2)	0.7 (0.5)
	v_5	0.2 (0.2)	<0.1 (0.2)	0.2 (0.2)	1 (3)
	v_6	5 (17)	11 (2)	5 (6)	0.9 (2)
	v_7	3 (3)	0.1 (0.4)	2 (4)	2 (2)
η symmetry	v_2	0.8 (0.7)	<0.1 (<0.1)	0.2 (0.1)	0.3 (<0.1)
	v_3	1 (1)	0.5 (0.3)	0.6 (0.5)	1 (0.5)
	v_4	1 (1)	0.4 (0.9)	2 (5)	4 (9)
	v_5	2 (2)	3 (5)	4 (4)	3 (3)
	v_6	10 (7)	4 (4)	11 (7)	11 (7)
	v_7	11 (15)	11 (15)	15 (12)	
centrality	v_2	1 (1)	1 (1)	0.5 (0.3)	1 (1)
	v_3	0.2 (0.2)	0.2 (<0.1)	0.3 (0.3)	0.7 (0.5)
	v_4	<0.1 (<0.1)	0.4 (0.7)	1 (3)	0.8 (3)
	v_5	2 (2)	0.2 (0.5)	4 (4)	2 (1)
	v_6	2 (1)	2 (2)	2 (3)	2 (3)
	v_7	11 (7)	8 (7)	4 (4)	4 (4)
residual sine term	v_2	0.2 (0.2)	0.1 (<0.1)	0.4 (0.5)	0.3 (0.5)
	v_3	0.5 (0.5)	1 (1)	2 (2)	1 (0.4)
	v_4	1 (2)	0.7 (1)	0.2 (3)	6 (4)
	v_5	3 (4)	0.1 (3)	11 (13)	11 (4)
	v_6	3 (11)	17 (21)	21 (31)	21 (31)
	v_7	34 (26)		35 (43)	
MC closure	v_2	2 (2)	1 (1)	0.3 (<0.1)	1 (1)
	v_3	2 (3)	2 (1)	14 (14)	11 (11)
	v_4	4 (4)	0.5 (1)	40-50%	
				1 (3)	5 (9)
				10-20%	
	v_5	3 (7)	14 (21)	8 (7)	2 (3)
	v_6	-	-	-	-
	v_7	-	-	-	-
residual FCal mis-calibration	v_2	0.1 (0.4)	0.7 (1)	0.1 (<0.1)	2 (0.6)
	v_3	1 (2)	2 (2)	0.3 (2)	8 (10)
	v_4	2 (3)	4 (6)	3 (2)	0.1 (6)
	v_5	8 (6)	<0.1 (4)	5 (8)	2 (3)
	v_6	17 (5)	5 (17)	28 (3)	28 (3)
	v_7	34 (13)	34 (13)	34 (13)	34 (13)

Table 2: The relative contributions to the systematic uncertainty of SP and EP (in parentheses) v_n measurements for v_n in selected bins of centrality and transverse momentum. The contributions are expressed in % and are rounded to two significant figures.

7 Results

7.1 p_{T} dependence

Figures 5 and 6 show the v_n obtained from the SP and 2PC methods, respectively, as a function of p_{T} for several centrality intervals. The SP results are integrated over the pseudorapidity $|\eta| < 2.5$. The 2PC results are obtained with $0.5<p_{\mathrm{T}}^{a}<5$ GeV and for $|\Delta\eta|>2$. The v_n values show a similar p_{T} dependence across all centralities: a nearly linear rise to about 2 GeV, followed by a gradual increase to reach a maximum around 2.5-3.5 GeV and a gradual fall at higher p_{T}. However, significant v_n values persist even at the highest measured p_{T} (~20 GeV), especially for v_2. In peripheral events, at the highest p_{T}, the 2PC-v_2 values again show an increasing trend due to the increasing influence of the away-side jet. The increased v_2 is accompanied by reduced values of v_3 and increased values of v_4, which is characteristic of a large away-side peak, as described in Section 5.1. This is most clearly seen in the (70–75)% centrality interval, where the 2PC v_2 values show a strong increase beyond $p_{\mathrm{T}} \sim 10$ GeV. The v_2 varies significantly with centrality, reflecting a change in the shape of the average initial collision geometry, from nearly circular in central collisions to an almond shape in peripheral events. The higher harmonics do not show similar behaviour, as neither higher-order eccentricities nor the fluctuations vary so significantly with the centrality. The v_2 is dominant at all centralities, except in the (0–5)% interval where at high p_{T} v_3 and v_4 become larger than v_2, indicating that the dominant source of observed flow comes from the initial geometry fluctuations. The v_4, similarly to v_2, exhibits an increase beyond $p_{\mathrm{T}} \sim 10$GeV, which can be attributed to the presence of the events with di-jets in the data. In the SP measurement the v_7 results are also presented. The characteristics of v_7 are similar to the other high-order harmonics, but the values are smaller and significant, given the uncertainties, only in central and mid-central collisions and for the p_{T} range of 2.5–3.5 GeV.

Figure 7 compares the v_n values measured with the EP and SP methods for the integrated p_{T} range of $0.5<p_{\mathrm{T}}<25$ GeV. A small difference is seen between the v_2 values measured with the two methods. The difference is largest in mid-central events: about 3% in the (20–30)% centrality interval, about 1% in the (0–5)% most central collisions and negligible in peripheral collisions. This difference is expected according to [37] as the SP method measures $\sqrt{\langle v_n^2 \rangle}$ while the EP method measures a value in between $\langle v_n \rangle$ and $\sqrt{\langle v_n^2 \rangle}$, with the former value attained in the limit of the correction factor (the inverse of the denominator in Eq. (9)) approaching unity and the latter when it is large. In the most central and peripheral events, where the correction is large for the second-order harmonic, the EP v_2 values are closer to the SP ones, while for the mid-central events where the correction is small, the EP v_2 values are systematically lower than the SP v_2 values. For higher-order harmonics, the difference between the EP and SP v_n values is consistent with zero, which implies that the EP measurements are always in the limit of large correction factor.

Figure 8 shows a comparison of the SP and 2PC results. There is significant difference between the v_2 values measured by the two methods in the (0–5)% centrality intervals, with the SP method giving consistently higher values. This difference decreases considerably for (20–30)% mid-central events, where the v_2 values match within 2–5% up to $p_{\mathrm{T}} \sim 10$ GeV. A roughly similar trend is observed in the higher-order harmonics, where the difference between the 2PC and SP v_n values is largest in the most central events, and decreases for mid-central events. For v_3 and v_4, where statistics allow for a clear comparison, the v_n values match within ~5% for $p_{\mathrm{T}} < 4$ GeV for the three centrality intervals shown in Figure 8. In principle both the SP and 2PC methods measure $\sqrt{\langle v_n^2 \rangle}$ and the v_n values measured by the two methods should be very similar. However, there are differences in the way the two methods are implemented in

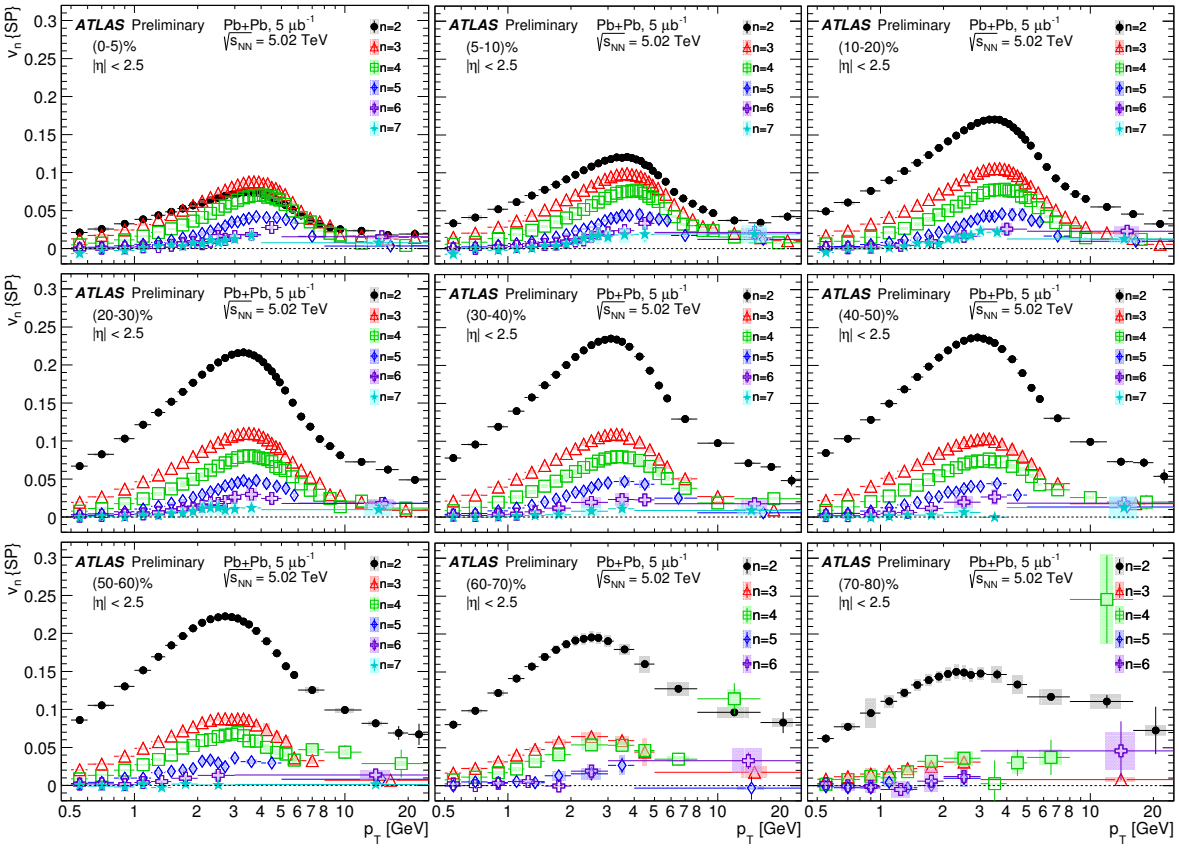

Figure 5: The v_n obtained with the SP method as a function of transverse momentum p_{T}, integrated over $|\eta| < 2.5$ in nine centrality intervals, from most central at the top left panel to most peripheral at the bottom right. For the (70–80)% centrality interval, only v_2, v_3 and v_4 are shown due to large statistical fluctuations for higher harmonics. Results are averaged over the intervals indicated by horizontal error bars. The vertical error bars indicate statistical uncertainties. The shaded bands indicate systematic uncertainties.

this analysis that can result in systematic differences in the measured v_n values. In general any breakdown of factorization (Eq. (5)) would result in systematic differences between the 2PC and SP results. Such factorization breakdown has been measured to be significant in central events [38]. Furthermore, in the 2PC method the η gap between the reference and associated particles is chosen to be $|\Delta\eta|>2$, while in the SP method - where the reference flow is measured in the FCal - the minimum gap between the tracks and the FCal is 3.2 units in η. The presence of longitudinal-flow fluctuations, in which the EP angle can change with η, can result in different v_n values depending on the η range where the reference flow is measured [39, 40]. This effect is also found to be larger in central events and relatively smaller in mid-central events [40]. These effects can lead to the observed difference between the SP and 2PC v_n values.

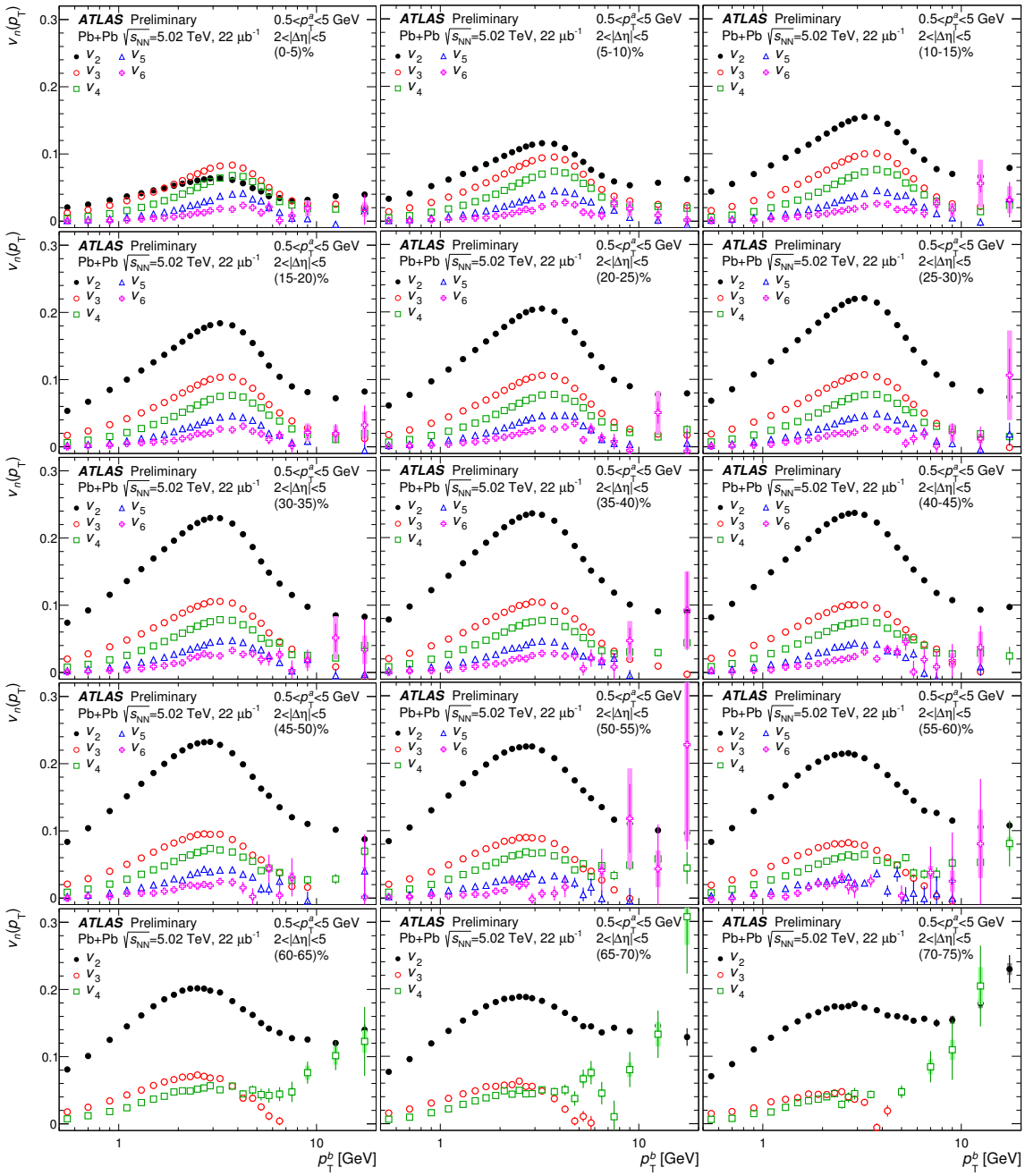

Figure 6: The v_n values obtained with the 2PC method as a function of p_{T}^b for $0.5<p_{\mathrm{T}}^a<5$ GeV. Each panel represents a different centrality interval. The vertical error bars indicate statistical uncertainties. The shaded bands indicate systematic uncertainties.

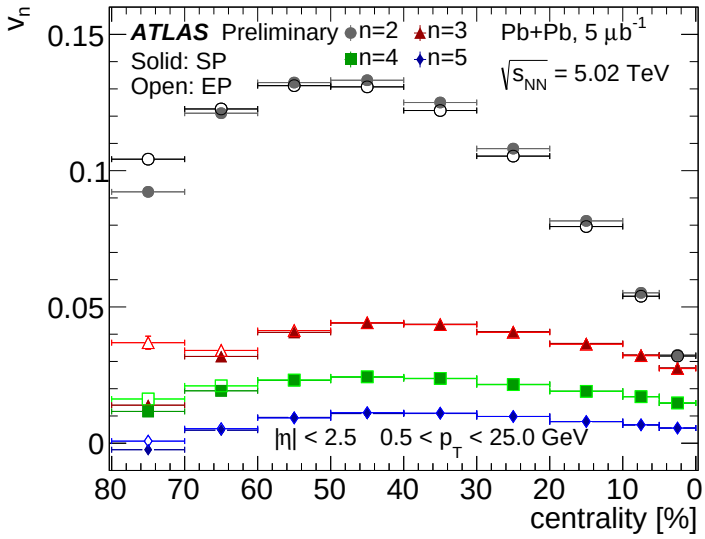

Figure 7: Comparison of the v_n obtained with EP and SP methods as a function of centrality. The results are integrated over $0.5<p_{\mathrm{T}}<25$ GeV and the entire available η range. Results are averaged over the intervals indicated by horizontal error bars. The vertical error bars indicate statistical uncertainties.

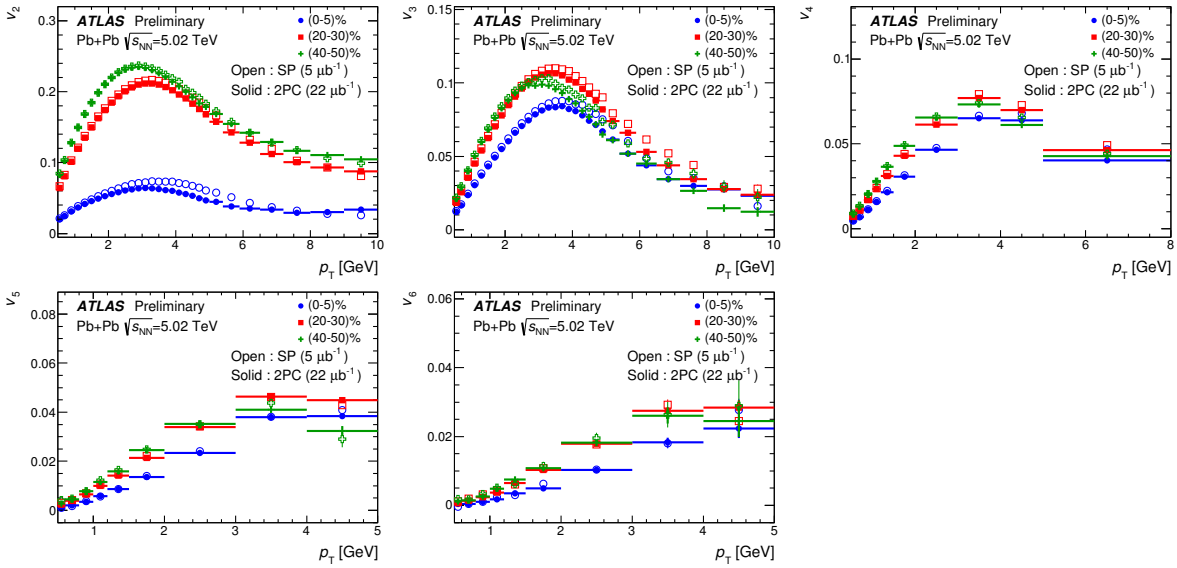

Figure 8: Comparison of the v_n obtained with 2PC and SP methods as a function of p_{T}. Each panel shows the comparison for a different order harmonic. The comparisons are shown for three different centrality intervals: (0–5)%, (20–30)% and (40–50)%. The horizontal bars indicate the widths of the p_{T} intervals over which the v_n values are measured, and are shown only for the 2PC data. The vertical error bars indicate statistical uncertainties.

7.2 η dependence

A weak η dependence of the v_n is shown in Figures 9 and 10 obtained for low- and high-p_{T} particles respectively. In the most central collision the distribution is consistent with a uniform distribution irrespective of the p_{T}. In mid-central collisions the integrated v_n over the p_{T} range from 2 to 3 GeV is higher by about 10% in at $\eta = 0$ as compared to $\eta = 2.5$ for all harmonics, while at low-p_{T} the variation is consistent with zero.

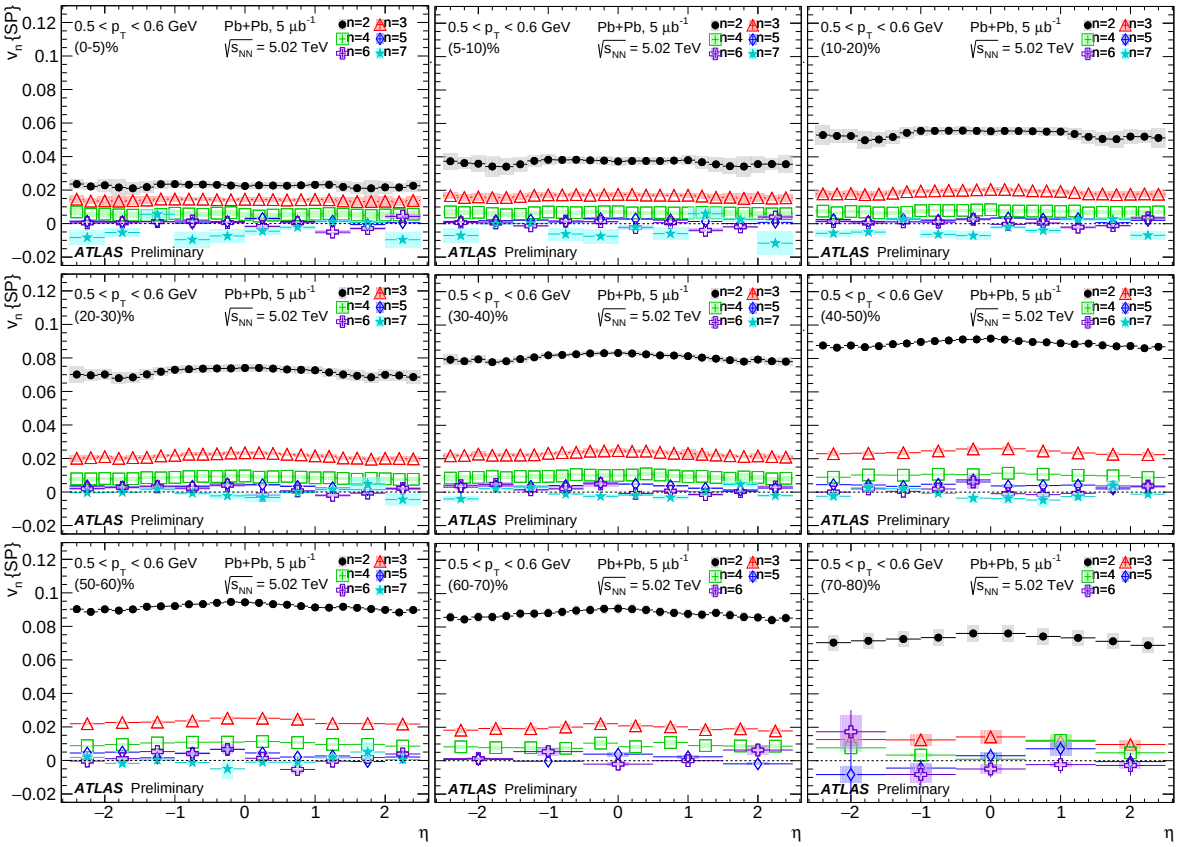

Figure 9: The v_n obtained with the SP method, integrated over $0.5 < p_{\mathrm{T}} < 0.6$ GeV, as a function of pseudorapidity. Each panel corresponds to a different centrality interval. Results are averaged over the intervals indicated by horizontal error bars. The vertical error bars indicate statistical uncertainties. The shaded areas indicate systematic uncertainties.

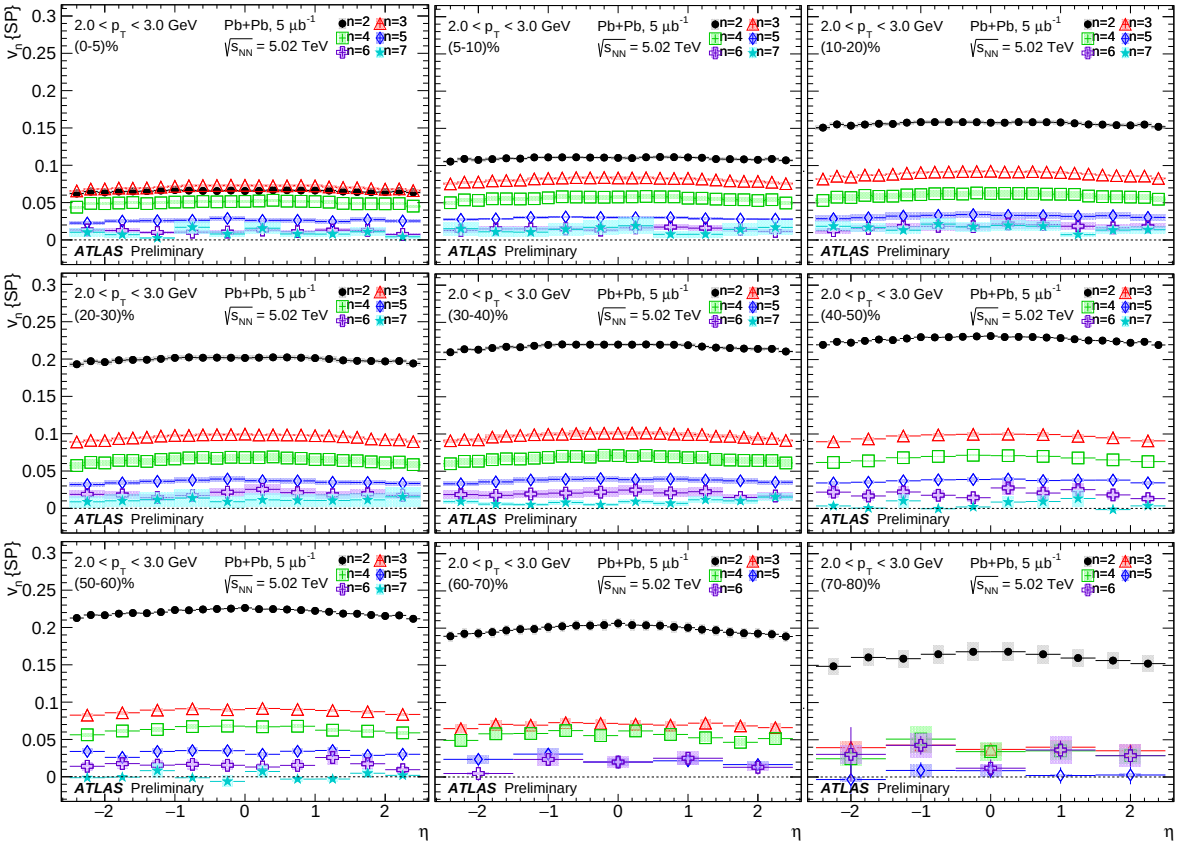

Figure 10: The v_n obtained with the SP method, integrated over $2 < p_{\mathrm{T}} < 3$ GeV, as a function of pseudorapidity. Each panel corresponds to a different centrality interval. Results are averaged over the intervals indicated by horizontal error bars. The vertical error bars indicate statistical uncertainties. The shaded areas indicate systematic uncertainties.

7.3 Centrality dependence

Figure 11 shows the centrality dependence of v_n integrated over $|\eta| < 2.5$ and for various ranges of p_{T} using the SP method. Except for the most central collisions (0–5)%, the elliptic flow is the dominant asymmetry. For $p_{\mathrm{T}} < 8$ GeV, a clear dependence on initial geometry can be observed as the v_2 is highest in mid-central collision, where this asymmetry is most significant. At $p_{\mathrm{T}} > 8$ GeV v_2 is still the dominant harmonic, and it is non-zero even in peripheral collisions as non-flow effects start to contribute to it. A hierarchy $v_{n+1} < v_n$ can be observed for harmonics from 3 to 7 for all ranges of p_{T} and all centralities.

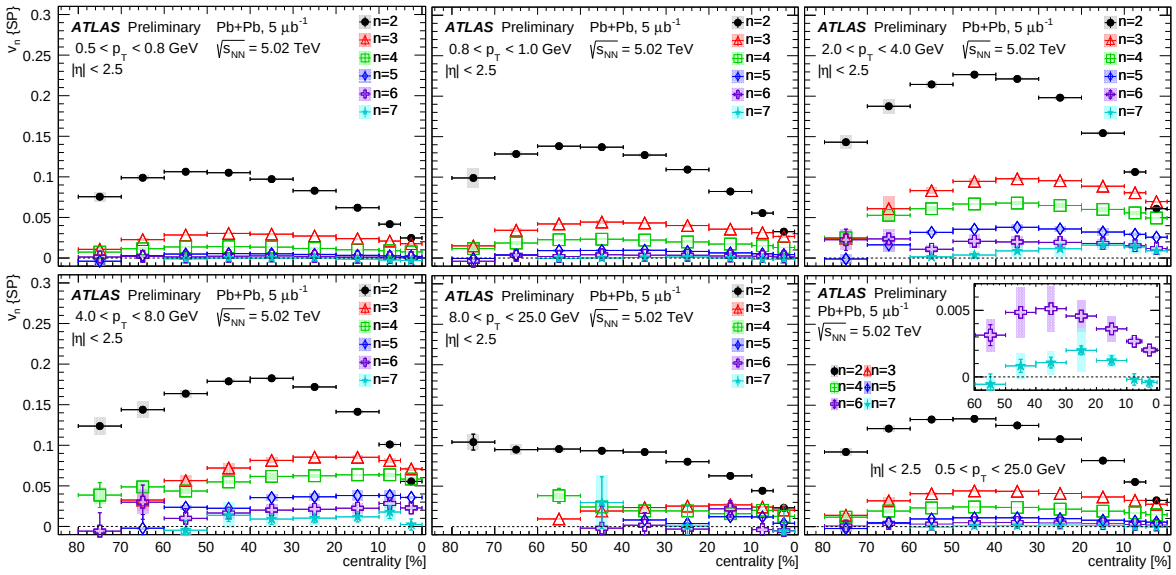

Figure 11: Integrated v_n {SP} vs. centrality for six p_{T} ranges shown in the panels from lowest p_{T} range at the top left to the highest at the bottom right extracted from the scalar product method. In the inset in bottom right panel the v_6 and v_7 integrated over $0.5 < p_{\mathrm{T}} < 25$ GeV are shown with adjusted scale. Results are averaged over the intervals indicated by horizontal error bars. The vertical error bars indicate statistical uncertainties. The shaded areas indicate systematic uncertainties.

7.4 Comparison to Pb+Pb results at $\sqrt{s_{\mathrm{NN}}}$ =2.76 TeV

Figure 12 shows a comparison of the v_n measured in the present analysis at $\sqrt{s_{\mathrm{NN}}} = 5.02$ TeV with the corresponding measurements at $\sqrt{s_{\mathrm{NN}}} = 2.76$ TeV for harmonics v_2 to v_6 obtained using the 2PC method. The comparisons are shown for two centralities: a central interval of (0–5)% and a mid-central interval of (20–30)%. Figure 13 shows a similar comparison of results obtained using EP method for (0–5)% and (40–60)% centrality bins. The v_n at the two energies are quite similar and almost throughout consistent within systematic and statistical uncertainties. These results are consistent with the recent ALICE measurements comparing the measurement of v_n at the two collision energies [41].

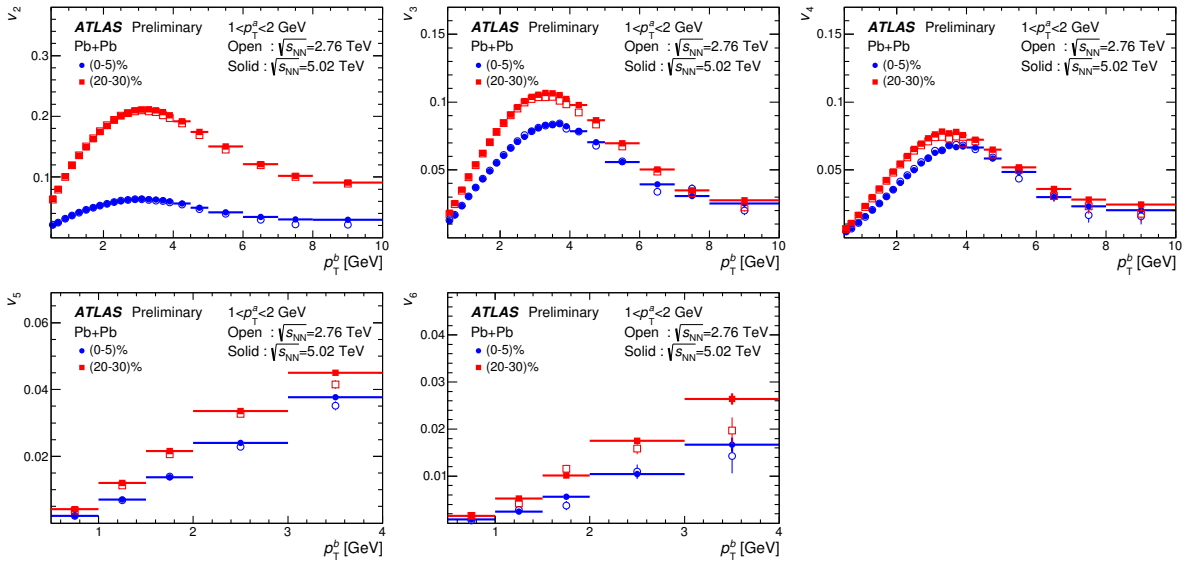

Figure 12: Comparisons of the 2PC-v_n measured at $\sqrt{s_{\rm NN}}$ =2.76 TeV (Run 1) and at $\sqrt{s_{\rm NN}}$ =5.02 TeV (Run 2). The results are plotted as a function of $p_{\rm T}^b$ for 1<$p_{\rm T}^a$ <2 GeV for two centralities: (0–5)% and (20–30)%. Each panel corresponds to a different harmonic. Results are averaged over the intervals indicated by horizontal error bars. The vertical error bars indicate statistical uncertainties.

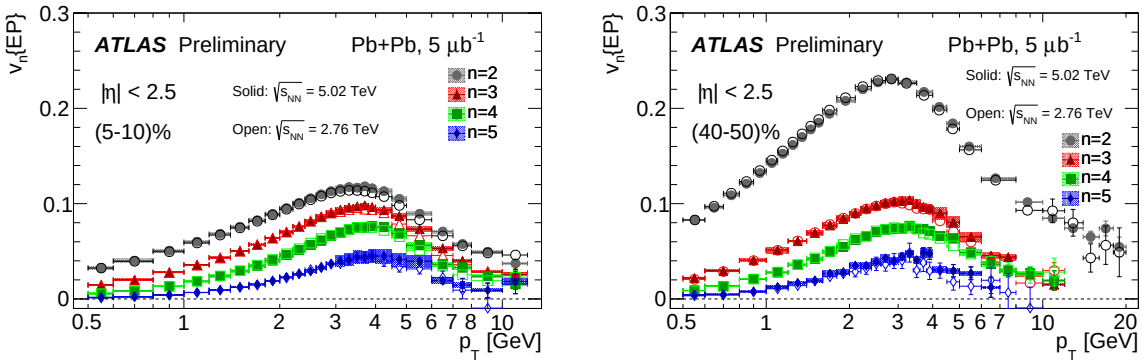

Figure 13: Comparison of the v_n obtained with EP method using Run 1 and Run 2 data as a function of $p_{\rm T}$. The results are shown in two centrality bins: (5–10)% and (40–50)%. Results are averaged over the intervals indicated by horizontal error bars. The vertical error bars indicate statistical uncertainties. The shaded areas indicate systematic uncertainties.

8 Summary

In summary, this note presents the first ATLAS measurements of azimuthal anisotropy of charged particles in Pb+Pb collisions at $\sqrt{s_{\rm NN}}$ =5.02 TeV using LHC Run 2 data. The measurements are done using an integrated luminosity of 5 μb^{-1} in SP/EP and 22 μb^{-1} in 2PC results. The azimuthal anisotropies, quantified by the flow harmonics v_n, are measured using the SP (n=2-7), EP (n=2-5) and 2PC (n=1-6) methods. The measurements are done over wide transverse momentum (0.5 < $p_{\rm T}$ < 25 GeV), pseudorapidity ($|\eta| < 2.5$) and centrality (0-80)% ranges. All harmonics show similar $p_{\rm T}$ dependence, first increasing with $p_{\rm T}$ up to a maximum around 3–4 GeV and then decreasing for higher $p_{\rm T}$. However, significant values of the

second-order harmonic v_2 persist up to 25 GeV, which is the highest p_{T} measured in this note. The high-p_{T} v_2 measured here can serve to improve understanding of partonic energy loss in the QGP. The elliptic flow signal is strongly dependent on event centrality and it is largest in mid-central events (30-50)%. The higher-order harmonics show a weak centrality dependence, which is consistent with an anisotropy associated with fluctuations in the initial geometry. The v_n coefficients are shown to exhibit only a weak η-dependence across all centrality intervals. The results obtained using the EP and SP methods are consistent for harmonics of order $n \geq 3$. A small, systematic difference is observed for v_2, where the values obtained from the SP method are up to 3% larger than the values obtained using the EP method. The 2PC and SP methods give values for v_n that are quite consistent up to $\sim$ 10 GeV. However, in the most central events the SP method gives systematically larger values for v_2 for $p_{\mathrm{T}} > 2$ GeV. Comparisons to measurements in Pb+Pb collisions at $\sqrt{s_{\mathrm{NN}}}$ =2.76 TeV show that the p_{T} dependence of the v_n shows no change from $\sqrt{s_{\mathrm{NN}}}$ =2.76 TeV to $\sqrt{s_{\mathrm{NN}}}$ =5.02 TeV.

References

[1] B. B. Back et al., *The PHOBOS perspective on discoveries at RHIC*, Nucl. Phys. **A757** (2005) 28–101, arXiv: nucl-ex/0410022 [nucl-ex].

[2] J. Adams et al., *Experimental and theoretical challenges in the search for the quark gluon plasma: The STAR Collaboration's critical assessment of the evidence from RHIC collisions*, Nucl. Phys. **A757** (2005) 102–183, arXiv: nucl-ex/0501009 [nucl-ex].

[3] I. Arsene et al., *Quark gluon plasma and color glass condensate at RHIC? The Perspective from the BRAHMS experiment*, Nucl. Phys. **A757** (2005) 1–27, arXiv: nucl-ex/0410020 [nucl-ex].

[4] K. Adcox et al., *Formation of dense partonic matter in relativistic nucleus-nucleus collisions at RHIC: Experimental evaluation by the PHENIX collaboration*, Nucl. Phys. **A757** (2005) 184–283, arXiv: nucl-ex/0410003 [nucl-ex].

[5] F. Karsch, *Properties of the Quark Gluon Plasma: A Lattice perspective*, Nucl. Phys. A783 **783** (2007) 13–22.

[6] J.-Y. Ollitrault, *Anisotropy as a signature of transverse collective flow*, Phys. Rev. D **46** (1 1992) 229–245.

[7] S. Voloshin and Y. Zhang, *Flow study in relativistic nuclear collisions by Fourier expansion of Azimuthal particle distributions*, Z. Phys. **C70** (1996) 665–672, arXiv: hep-ph/9407282 [hep-ph].

[8] ALICE Collaboration, *Elliptic Flow of Charged Particles in Pb-Pb Collisions at* $\sqrt{s_{NN}} = 2.76$ TeV, Phys. Rev. Lett. **105** (25 2010) 252302.

[9] ATLAS Collaboration, *Measurement of the pseudorapidity and transverse momentum dependence of the elliptic flow of charged particles in lead–lead collisions at* $\sqrt{s_{\mathrm{NN}}} = 2.76$ *TeV with the ATLAS detector*, Phys. Lett. B **707** (2012) 330, arXiv: 1108.6018 [hep-ex].

[10] ATLAS Collaboration, *Measurement of the azimuthal anisotropy for charged particle production in* $\sqrt{s_{\mathrm{NN}}} = 2.76$ *TeV lead–lead collisions with the ATLAS detector*, Phys. Rev. C **86** (2012) 014907, arXiv: 1203.3087 [hep-ex].

[11] CMS Collaboration, *Measurement of the elliptic anisotropy of charged particles produced in PbPb collisions at* $\sqrt{s_{\mathrm{NN}}} = 2.76$ *TeV*, Phys. Rev. C **87** (2013) 014902, arXiv: 1204.1409 [hep-ex].

[12] A. M. Poskanzer and S. Voloshin, *Methods for analyzing anisotropic flow in relativistic nuclear collisions*, Phys.Rev. **C58** (1998) 1671–1678, arXiv: nucl-ex/9805001 [nucl-ex].

[13] S. A. Voloshin, A. M. Poskanzer and R. Snellings, *Collective phenomena in non-central nuclear collisions*, (2008), arXiv: 0809.2949 [nucl-ex].

[14] ATLAS Collaboration, *Measurement of flow harmonics with multi-particle cumulants in Pb+Pb collisions at* $\sqrt{s_{\mathrm{NN}}} = 2.76$ *TeV with the ATLAS detector*, Eur. Phys. J. C **74** (2014) 3157, arXiv: 1408.4342 [hep-ex].

[15] STAR Collaboration, J. Adams et al., *Azimuthal anisotropy in Au+Au collisions at s(NN)**(1/2) = 200-GeV*, Phys. Rev. **C72** (2005) 014904, arXiv: nucl-ex/0409033 [nucl-ex].

[16] PHENIX Collaboration, A. Adare et al.,
Azimuthal anisotropy of neutral pion production in Au+Au collisions at $\sqrt{(}s_N N) = 200$ *GeV: Path-length dependence of jet quenching and the role of initial geometry*,
Phys. Rev. Lett. **105** (2010) 142301, arXiv: 1006.3740 [nucl-ex].

[17] ALICE Collaboration, *Elliptic flow of charged particles in Pb-Pb collisions at 2.76 TeV*,
Phys. Rev. Lett. **105** (2010) 252302, arXiv: 1011.3914 [nucl-ex].

[18] CMS Collaboration, *Measurement of the elliptic anisotropy of charged particles produced in PbPb collisions at* $\sqrt{s_{NN}}$*=2.76 TeV*, Phys. Rev. **C87** (2013) 014902,
arXiv: 1204.1409 [nucl-ex].

[19] ATLAS Collaboration, *The ATLAS Experiment at the CERN Large Hadron Collider*,
JINST **3** (2008) S08003.

[20] ATLAS Collaboration, 'ATLAS Insertable B-Layer Technical Design Report',
tech. rep. CERN-LHCC-2010-013. ATLAS-TDR-19,
URL: http://cds.cern.ch/record/1291633.

[21] ATLAS Collaboration, 'ATLAS Insertable B-Layer Technical Design Report Addendum',
tech. rep. CERN-LHCC-2012-009. ATLAS-TDR-19-ADD-1,
Addendum to CERN-LHCC-2010-013, ATLAS-TDR-019: CERN, 2012,
URL: http://cds.cern.ch/record/1451888.

[22] ATLAS Collaboration, *The ATLAS Inner Detector commissioning and calibration*,
Eur. Phys. J. C **70** (2010) 787, arXiv: 1004.5293 [hep-ex].

[23] ATLAS Collaboration, *Performance of the ATLAS Trigger System in 2010*,
Eur. Phys. J. C **72** (2012) 1849, arXiv: 1110.1530 [hep-ex].

[24] M. L. Miller et al., *Glauber modeling in high energy nuclear collisions*,
Ann. Rev. Nucl. Part. Sci. **57** (2007) 205–243, arXiv: nucl-ex/0701025 [nucl-ex].

[25] X.-N. Wang and M. Gyulassy,
HIJING: A Monte Carlo model for multiple jet production in pp*,* pA*, and* AA *collisions*,
Phys. Rev. D **44** (11 1991) 3501–3516.

[26] J. Jia and S. Mohapatra, *Disentangling flow and nonflow correlations via Bayesian unfolding of the event-by-event distributions of harmonic coefficients in ultrarelativistic heavy-ion collisions*,
Phys. Rev. **C88** (2013) 014907, arXiv: 1304.1471 [nucl-ex].

[27] S. Agostinelli et al., GEANT4 Collaboration, *GEANT4: A simulation toolkit*,
Nucl. Instrum. Meth. **A 506** (2003) 250.

[28] ATLAS Collaboration,
'The Optimization of ATLAS Track Reconstruction in Dense Environments',
tech. rep. ATL-PHYS-PUB-2015-006, URL: http://cdsweb.cern.ch/record/2002609.

[29] ATLAS Collaboration, *Measurement of the distributions of event-by-event flow harmonics in lead–lead collisions at* $\sqrt{s_{\mathrm{NN}}} = 2.76$ *TeV with the ATLAS detector at the LHC*,
JHEP **11** (2013) 183, arXiv: 1305.2942 [hep-ex].

[30] ATLAS Collaboration, *Observation of Associated Near-Side and Away-Side Long-Range Correlations in* $\sqrt{s_{\mathrm{NN}}} = 5.02$ *TeV Proton–Lead Collisions with the ATLAS Detector*,
Phys. Rev. Lett. **110** (2013) 182302, arXiv: 1212.5198 [hep-ex].

[31] ATLAS Collaboration, *Measurement of long-range pseudorapidity correlations and azimuthal harmonics in* $\sqrt{s_{\rm NN}} = 5.02$ *TeV proton–lead collisions with the ATLAS detector*, Phys. Rev. C **90** (2014) 044906, arXiv: 1409.1792 [hep-ex].

[32] ATLAS Collaboration, *Measurement of the correlation between flow harmonics of different order in lead–lead collisions at* $\sqrt{s_{\rm NN}} = 2.76$ *TeV with the ATLAS detector*, Phys. Rev. C **92** (2015) 034903, arXiv: 1504.01289 [hep-ex].

[33] ATLAS Collaboration, *Observation of Long-Range Elliptic Azimuthal Anisotropies in* $\sqrt{s} = 13$ *and* 2.76 *TeV pp Collisions with the ATLAS Detector*, Phys. Rev. Lett. **116** (2016) 172301, arXiv: 1509.04776 [hep-ex].

[34] PHENIX Collaboration, A. Adare et al., *Dihadron azimuthal correlations in Au+Au collisions at* $\sqrt{s_{\rm NN}} = 200$*-GeV*, Phys. Rev. **C78** (2008) 014901, arXiv: 0801.4545 [nucl-ex].

[35] M. A. Lisa et al., *Femtoscopy in relativistic heavy ion collisions*, Ann. Rev. Nucl. Part. Sci. **55** (2005) 357–402, arXiv: nucl-ex/0505014 [nucl-ex].

[36] STAR Collaboration, C. Adler et al., *Elliptic flow from two and four particle correlations in Au+Au collisions at s(NN)**(1/2) = 130-GeV*, Phys.Rev. **C66** (2002) 034904, arXiv: nucl-ex/0206001 [nucl-ex].

[37] M. Luzum and J.-Y. Ollitrault, *Eliminating experimental bias in anisotropic-flow measurements of high-energy nuclear collisions*, Phys.Rev. **C87** (2013) 044907, arXiv: 1209.2323 [nucl-ex].

[38] CMS Collaboration, *Studies of azimuthal dihadron correlations in ultra-central PbPb collisions at* $\sqrt{s_{\rm NN}} = 2.76$ *TeV*, JHEP **02** (2014) 088, arXiv: 1312.1845 [hep-ex].

[39] J. Jia and P. Huo, *A method for studying the rapidity fluctuation and decorrelation of harmonic flow in heavy-ion collisions*, Phys. Rev. **C90** (2014) 034905, arXiv: 1402.6680 [nucl-th].

[40] CMS Collaboration, *Evidence for transverse-momentum- and pseudorapidity-dependent event-plane fluctuations in PbPb and pPb collisions*, Phys. Rev. C **92** (2015) 034911, arXiv: 1503.01692 [hep-ex].

[41] ALICE Collaboration, *Anisotropic flow of charged particles in Pb-Pb collisions at* $\sqrt{s_{\rm NN}} = 5.02$ *TeV*, Phys. Rev. Lett. **116** (2016) 132302, arXiv: 1602.01119 [nucl-ex].